Comparison between *ab initio* theory and scanning tunneling microscopy for (110) surfaces of III-V semiconductors

B. Engels, P. Richard, K. Schroeder, S. Blügel, Ph. Ebert, and K. Urban
Institut für Festkörperforschung, Forschungszentrum Jülich GmbH, 52425 Jülich, Germany
(Received 23 December 1997; revised manuscript received 1 June 1998)

We compare results of *ab initio* electronic structure calculations using density-functional theory with measured scanning tunneling microscopy (STM) images for the clean (110) surface of III-V semiconductors. A detailed analysis is made of the nature of the wave functions contributing to STM images. The atomic structure has been determined by total-energy minimization combined with the plane-wave pseudopotential technique. The nature of the wave functions (surface localization, surface resonance, or bulklike) has been determined for energies in the range of 3 eV on both sides of the fundamental gap. In particular, the decay of the density profiles into the vacuum as well as into the bulk has been analyzed. A consistent understanding of the voltage-dependent STM images has been obtained. For tunneling out of the occupied states the dangling bond at the anion gives the main contribution for all voltages measured. On the other hand, for tunneling into the empty states the dangling bond at the cation is important only for small voltages. For higher voltages resonances (backbond but also some bridgebond contributions) dominate the STM image, yielding the observed rotation of the apparent row direction. [S0163-1829(98)08735-9]

I. INTRODUCTION

The functioning of modern electronic devices is to a large extent based on the electronic properties of interfaces. Therefore, much research has been devoted to developing the best possible methods for controlling the fabrication and understanding the properties of interfaces. It turned out that the properties are strongly influenced by the cleanliness, geometrical structure, and electronic details of the bare surface of the semiconductor substrate. Understanding the electronic structure of surfaces and relating specific features to the atomic structure is thus of major interest. The GaAs(110) surface gained particular importance as a model surface, because GaAs can be cleaved in ultrahigh vacuum to expose a clean surface with a very low defect concentration. (110) cleavage surfaces of III-V compound semiconductors and their metallic overlayers are among the best understood surfaces: In the early years the research focused on the determination of the geometric structure, mostly by low-energy electron diffraction (LEED),[1–13] electron energy-loss spectroscopy (EELS),[14] and photoemission spectroscopy.[15–21] These experiments resulted in the proposal of the bond-rotation model:[22] The surface energy is minimized by an outward relaxation of the group-V atoms (anions, e.g., phosphorus atoms) relative to the group-III atoms (cations, e.g., indium atoms), while the dimension of the unit cell remains unchanged compared to the bulk. The relaxation corresponds to a buckling of the surface bond between the anion and cation by about 30°. The relaxation is closely connected with the absence of surface states in the fundamental band gap.[23,24] Two dangling bond states exist, one in the top part of the valence band and the other in the bottom part of the conduction band. After the invention of scanning tunneling microscopy (STM) it was even possible to show that the occupied and empty states are spatially shifted, because they are localized at the surface anion and cation, respectively.[25–27] These observations were corroborated by numerous calculations[28–37] improving over the years with the increasing availability of more detailed experimental data. However, rarely has a comparison between theory and experiment been attempted that goes beyond the buckling relaxation and the associated dangling bond states.

However, a detailed comparison of the currently available theoretical description of the surface with STM experiments unravels unclear features.[37,38] In fact, when the surface morphology measured in STM images is only explained on the level of the dangling bond states many details remain vague. This lack of knowledge hampers the interpretation of ongoing experimental developments such as the intensive investigations of point defects and impurities[39–51] as well as of heterostructures[52–57] by cross-sectional STM on the (110) cleavage surfaces. These STM measurements demonstrated the need for further improvements of the theoretical understanding. In particular, the analysis of ternary compounds, impurities, point defects, and the contrast close to interfaces in STM images has not yet reached a sufficient or acceptable level. Many technologically relevant questions must remain unanswered, unless a reliable theoretical background can be provided. Currently many theoretical calculations provide data, the accuracy of which is never verified experimentally. Developing ''rules'' for testing or comparing the theoretical results with STM experiments could decisively advance this field.

In this paper we demonstrate that current state of the art electronic structure calculations based on the density-functional theory in the local-density approximation (DFT-LDA) can help to clarify the role of the electronic structure of surfaces in STM imaging with atomic-scale resolution. The improvements are illustrated for the (110) surfaces of III-V compound semiconductors, where we find an excellent agreement with experiments. The *ab initio* computed electronic structure is compared with complementary scanning tunneling microscope (STM) experiments achieving the

highest lateral resolution possible. The comparison with high-resolution STM images improves considerably, if the supercell used in the calculation accounts reasonably for the decay of surface resonances into the bulk ($\gtrsim$17 layers crystal) and allows an accurate description of the decay of the states into the vacuum (seven layers of vacuum). We provide rules for the simulation of STM images in the Tersoff-Hamann scheme using the DFT-LDA by presenting a complete energy dependent analysis of the states, their decay into the vacuum, and their spatial distribution. Our combined theoretical and experimental study allows us to identify the contributions of surface resonances in STM images as a function of applied voltage: In contrast to the general belief the empty state images are dominated by surface resonances and not by the dangling bond state. The occupied surface resonances also contribute significantly, particularly at higher magnitudes of negative voltages. However, the resonances do not change much the morphology of the STM images, because they overlap spatially with the dangling bond state.

II. COMPUTATIONAL PROCEDURE

A. Electronic structure calculations

The electronic structure calculations are based on the density-functional theory in the local-density approximation.[58] They are combined with the plane-wave pseudopotential technique.[59,60] The Kosugi-Davidson iteration procedure[61] was used to solve the electronic eigenvalue problem; self-consistency was achieved with a Broyden quasi-Newton method in the generalized Anderson form.[62] The structural relaxation of the surface atoms was obtained from a total-energy minimization guided by Hellman-Feynman forces acting on the atoms. A modified Broyden-Fletcher-Goldfarb-Shano quasi-Newton scheme[63] was used for the determination of the minimum-energy configuration. The semi-infinite surface was modeled with a repeated slab. The relaxed surface structure was determined for a supercell consisting of a nine-layer slab separated by a vacuum region equivalent to a distance of seven layers. The positions of the atoms in the central layer were bulklike and fixed. Since typical surface resonances extend deep into the bulk, the conventional supercells consisting of up to nine (110) planes were found to be too small to yield accurate results. Thus we used in the electronic structure calculations a supercell of 17 (110) planes and a vacuum region equivalent to seven layers. The larger supercell was constructed by inserting eight additional bulklike layers into the relaxed supercell (of nine layers). This turned out to be sufficient to guarantee the decoupling of the two surfaces of the slab as indicated by the degeneracy of the eigenvalues for the symmetric and antisymmetric combination of most of the surface states, which was better than 1 and 200 meV for the bridgebond and backbond resonances, respectively [see Chap. 4(b)]. The electronic structure calculations were carried out with norm-conserving separable pseudopotentials and a set of plane-wave basis functions up to a kinetic energy of 12.25 Ry. For the determination of the self-consistent electron density a $4\times4\times2$ Monkhorst-Pack $\mathbf{k}$ point set has been used.[64,65] With the C_{2v} symmetry of the surface supercell this set reduces to four $\mathbf{k}$ points in the irreducible wedge of the Brillouin zone. To simulate the STM images we determined the local density of states and the spatial distribution of the wave functions in the vacuum region using 36 equidistant $\mathbf{k}_{\|}$ points in the irreducible part of the two dimensional (110) surface Brillouin zone $(\mathbf{k}_{mn}=\pi/a_0\times(0.1\times m\times[1,0]+0.1\times n\times[0,1]);\ m,n=0,1,...,5)$. A study of Hörmandinger *et al.*[66] and in more detail by Heinze and Blügel[67] shows the sensitivity of the corrugation of the local density of states (LDOS) on the $\mathbf{k}$ point distribution. It is important to use $\mathbf{k}$ points up to the boundary of the Brillouin zone. Table I shows the parameters used for the construction of the pseudopotentials. The pseudopotentials for all elements were constructed according to the Vanderbilt scheme.[68] Further details of the algorithms and calculational procedures employed can be found in Ref. 69.

TABLE I. Parameters used for the construction of the pseudopotentials according to the Vanderbilt scheme (Ref. 64). r_s, r_p, and r_d are the cutoff radii for *s,p,d* pseudoatom wave functions. The *s* and *p* pseudopotentials are generated with the ground states of the respective atoms, and the *d* pseudopotentials with the excited ionic configurations shown.

Element	r_s (a.u.)	r_p (a.u.)	r_d (a.u.)	Excited configuration
Al	1.15	1.25	1.25	[Ne] $3s^{1.2}3p^{0.6}3d^{0.2}$
In	1.15	1.25	1.25	[Kr $4d^{10}$] $5s^{1.2}5p^{0.6}5d^{0.2}$
P	1.15	1.25	1.25	[Ne] $3s^{1.8}3p^{1.8}3d^{0.4}$
As	1.15	1.25	1.25	[Ar $3d^{10}$] $4s^{1.8}4p^{1.8}4d^{0.4}$

B. Computation of theoretical STM images

The tunnel current I can be calculated using Bardeen's transfer Hamiltonian method.[70–72] In the limit of $k_BT\to0$ the tunneling current I as a function of the bias voltage V is given by

$$I(V)=\frac{4\pi e}{\hbar}\int_0^{eV}d\epsilon\,\rho^T(E_F^T-eV+\epsilon)\times\rho^S(E_F^S+\epsilon)\,|M(E_F^S+\epsilon,E_F^T-eV+\epsilon)|^2, \quad (1)$$

where ρ^S and ρ^T are the density of states of surface and tip, respectively. The energies ϵ are measured with respect to the Fermi energies E_F^S and E_F^T of the tip and the surface, respectively. The transfer matrix element M can be expressed as an integral over a separating surface Σ between crystal surface S and tip T:

$$M=M(\epsilon_\mu,\epsilon_\nu)=-\frac{\hbar}{2m}\int_\Sigma d\mathbf{S}(\Psi_\nu^{T*}\nabla\Psi_\mu^S-\Psi_\mu^S\nabla\Psi_\nu^{T*}), \quad (2)$$

where m is the electron mass. Ψ_μ^S and Ψ_ν^T are the wave functions of the surface and tip with eigenvalues ϵ_μ and ϵ_ν, respectively. The surface and the tip system is assumed to be well separated and interaction free. For further calculations one needs information about the wave functions of the tip that contribute to the tunnel current. The simplest approximation was introduced by Tersoff and Hamann,[70] who assumed *s* character for the tip wave functions:

$$\Psi_S^T(\mathbf{r}) = \frac{C}{\kappa r}\, e^{-\kappa r}, \quad r = |\mathbf{r}-\mathbf{R}| \tag{3}$$

with the decay constant κ and a normalization constant C. The explicit expression for the square of the matrix element then involves the occupation probability of the surface wave functions $\Psi_\mu^S(\mathbf{R})$ at the position $\mathbf{R}$ of the tip:

$$|M|^2 = \left(\frac{2\pi C\hbar^2}{\kappa m}\right)^2 |\Psi_\mu^S(\mathbf{R})|^2. \tag{4}$$

If, in addition, one assumes a smooth (nearly energy independent) DOS of the tip in the important energy interval around the Fermi energy [$\rho^T(\epsilon) = \text{const}$] the tunnel current can be expressed by the LDOS $\rho_{\text{lok}}^S(\mathbf{R},\epsilon)$ of the crystal surface evaluated at the position $\mathbf{R}$ of the tip:

$$I(\mathbf{R},V) = \frac{16\pi^3 C^2\hbar^3 e}{\kappa^2 m^2}\, \rho^T \int_0^{eV} d\epsilon\; \rho_{\text{lok}}^S(\mathbf{R}, E_F^S + \epsilon), \tag{5}$$

$$\rho_{\text{lok}}^S(\mathbf{R},\epsilon) = \sum_\mu |\Psi_\mu^S(\mathbf{R})|^2\, \delta(\epsilon - \epsilon_\mu), \tag{6}$$

where Ψ_μ^S are the calculated self-consistent wave functions of the surface supercell. This is the basis of our calculation of the tunnel current.

We have calculated eigenfunctions with eigenvalues in the valence and conduction bands at 36 equidistant $\mathbf{k}$ points in the irreducible part of the surface Brillouin zone and performed the summation over μ and ϵ explicitly. For very small voltages V the tunnel current is proportional to the applied voltage as derived by Tersoff and Hamann,[70] but the integral formulation of Eq. (1) should hold for voltages smaller than the work function ($\Phi = \Phi_{\text{vacuum}} - E_F$). We use the unperturbed slab wave functions to calculate the surface LDOS for voltages up to about half the work function. For the *p*-doped InP(110) surface (Fermi level at the valence-band maximum) the work function is 5.8 eV.[73] The major perturbation due to the applied voltage is the change of the functional form of the vacuum barrier. The modified vacuum barrier affects the decay of the wave functions into the vacuum quantitatively, but not qualitatively.[74] Therefore it is difficult to calculate the distance dependence of the tunnel current and to correlate this to the experimental distance dependences. However, we are mostly interested in the lateral variation of the tunnel current when we simulate the STM images. An additional difficulty arises from the use of the density-functional theory in the local-density approximation. In is known that the LDA cannot reproduce the correct electron potential far away from the surface since it does not contain the image potential. This means that the wave functions far away from the surface do not have the correct z dependence (z is the coordinate perpendicular to the surface) at large distances. Experience with the calculation of the LEED fine structure shows that the potential is quite well reproduced by the LDA up to distances of 10 a.u.[75] In our case we simulate the STM images at a distance of about 6 a.u. Furthermore, Jennings and co-workers[75] have shown that the lateral variation of the wave functions, which determines the regular LEED spots and in our case the topology of the STM images, is even less affected by the neglect of the image potential. As can be seen from Eqs. (5) and (6), all states contribute to the current whose energy is in the energy window $[E_F, E_F + eV]$. The weight of their contribution is the probability density $|\Psi_\mu^S(\mathbf{R})|^2$ at the position of the tip $\mathbf{R}$.

From Eqs. (5) and (6) it becomes obvious that the typical constant-current STM images show surfaces of constant energy-integrated LDOS (if the work function does not change laterally). Below, we compute the lateral variation of the energy integrated LDOS at a *fixed distance from the surface*. These *theoretical* ''constant distance'' STM images are thus images of the variation of the LDOS in the vacuum. Since the distance dependence of the tunnel current is exponential and the lateral variation is small compared to the average value, the theoretical ''constant distance images'' are to first order equivalent with ''constant current images,'' which are measured experimentally.

III. EXPERIMENTS

The electronic structure of (110) cleavage surfaces of InP and GaP was probed with the scanning tunneling microscope. The doping levels of the investigated crystals were Zn:$(1.3-2.1)\times 10^{18}$ and Sn:$(0.9-1.8)\times 10^{18}$ cm^{-3} for InP and Zn:$(1.7-5.8)\times 10^{17}$ and S:$(5.6-6)\times 10^{17}$ cm^{-3} for GaP. Single crystals were cleaved in ultrahigh-vacuum (UHV) [$(0.5-1)\times 10^{-8}$ Pa] using a double-wedge technique and immediately transferred without breaking of the vacuum to the scanning tunneling microscope in a separate UHV chamber. In order to obtain the highest possible resolution we used two separate very stable modified Besocke-type STM's at room temperature.[76] The tips were etched electrochemically with NaOH from polycrystalline tungsten wire. They usually have a radius of curvature of about 5 nm as determined by transmission electron microscopy. Each tip was conditioned by either *ex situ or in situ* field emission prior to any use. The samples were contacted using special gold contacts: gold was sputtered on two opposite faces of the samples and a capacitance was discharged several times over the two gold contacts prior to the evaporation of a second and final gold layer. These contacts have perfect Ohmic characteristics. For the analysis of the electronic structure of the surface, we measured high-resolution constant-current images of the empty and occupied states at tunneling voltages ranging from -4.5 to $+3.5$ V. Particular care was taken to avoid double-tip images or any other disturbing imaging artifacts.

IV. COMPUTATION OF THE RELAXATION OF THE SURFACE ATOMS

The first step toward a calculation of the electronic properties of the surface is the determination of the atomic configuration of the uppermost surface layers. Experimentally it has been shown that the relaxation of the positions of atoms is relatively simple on (110) surfaces of cubic III-V compound semiconductors. The anions (group-V atoms) relax out of the surface (upward movement) relative to the surface cations without a significant change of the bond lengths.[1–13] This results in a buckled surface with a buckling angle close to 30°. It has been suggested that the preferred planar threefold coordination with occupied sp^2-like and empty p_z-like

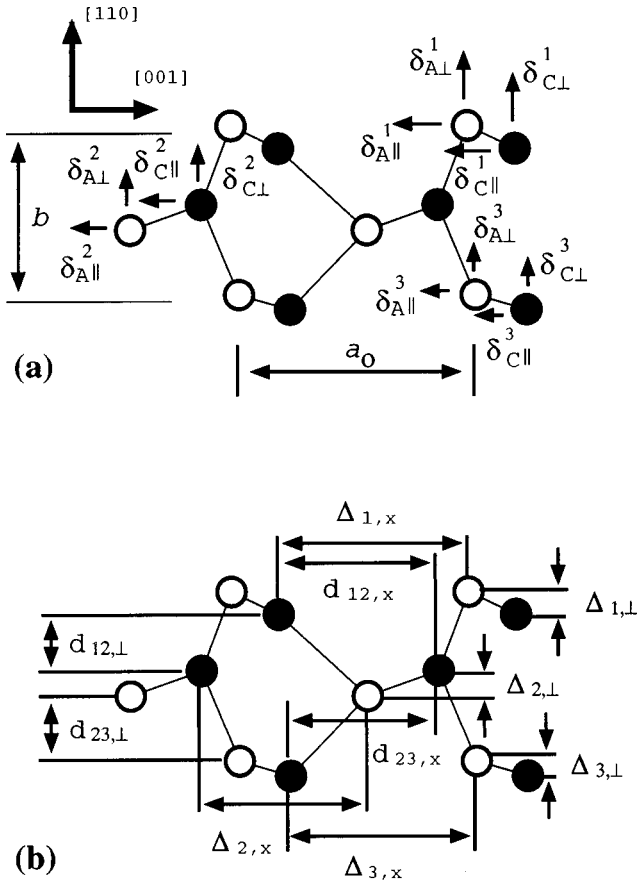

FIG. 1. Parameters used to characterize the structure of the buckled (110) surfaces of III-V semiconductors. The circles denote the sites of anions *A* (empty circles, e.g., P) and cations *C* (filled circles, e.g., In) projected to the plane shown. Because of symmetry, displacements occur only in the plane shown. (a) shows the definitions of the displacements of surface and subsurface atoms with respect to the extrapolated unrelaxed bulk positions. a_0 = cubic lattice constant, $b = a_0/\sqrt{2}$, the nearest-neighbor distance of equal atoms in the bulk. (b) shows the definitions of the relative distances of the relaxed atoms.

orbitals at the cations (group-III atoms) and the three-dimensional (incomplete) tetrahedral coordination with sp^3-like orbitals at the anions are the driving forces of the relaxation.[2,3,77,78] Figure 1 shows a schematic side view of the relaxed surface including the conventional notation of the atomic displacements (structural parameters). The upper and lower parts of Fig. 1 show the absolute and relative displacements, respectively. There are two reasons for the use of two sets of structural parameters. First, the relative displacements converge faster than the absolute displacements with the thickness of the slab and the number of layers allowed to relax. For a slab of five layers the buckling and the distances in the first two layers are converged already, whereas the absolute coordinates are influenced by the small displacements of further subsurface layers in thicker slabs. Second, the data given in the literature are in many cases incomplete sets of relative displacements, which do not allow us to calculate the absolute values of the atomic displacement. The absolute values, however, include the full information and thus should be taken as reference.

The convergence of the structural relaxations yielding the minimum total-energy configuration was tested using the AlAs(110) surface. We analyzed the effects of the size of the supercell, the number of **k** points used, and the number of layers allowed to relax. The size of the vacuum was equivalent to seven layers for all calculations. It was sufficiently large in order to avoid any overlap of the wave functions from the two surfaces of the slab in the vacuum region. The wave functions were found to decay below the numerical detection limit within less than 10 a.u., i.e., 2.5-layer distances. The tests were performed with plane-wave basis functions up to a kinetic energy of 12.25 Ry. For AlAs we tested the sensitivity of the atomic relaxation on the number of **k** points used. The differences in the relaxations of the upper two atomic layers for $4\times4\times2$, $4\times4\times4$, and $6\times6\times2$ Monkhorst-Pack **k** point sets are less than 10^{-3} a.u., (1 a.u.$=0.052\,917\,7$ nm). To ensure the same **k** point density for the surface and bulk calculations, we have optimized the lattice constant of the bulk in the same unit cell but with a full slab (no vacuum). The optimization was achieved by minimizing the cell energy for isotropic deformation, i.e., for constant ratios of the lattice constants of the tetragonal cell. We found that the main features of the system are already reproduced well with the smallest set of **k** points ($4\times4\times2$ **k** points in the Brillouin zone of the supercell,[64,65] equivalent to four **k** points in the irreducible wedge of the two-dimensional Brillouin zone). We only use this set of **k** points in the following calculations. The absolute positions of the surface atoms depend on the number of layers allowed to relax. We tested five layers (four layers relaxed on both sides), seven layers (six layers relaxed), and nine layers (eight layers relaxed). The surface atoms respond to the relaxation of the lower subsurface layers. However, the relative positions of the atoms in the upper two layers (distances and buckling angle) are already well described in the five layer slab with relative differences of less than 10^{-3} compared to thicker slabs. For the final determination of the relaxation we used the largest supercell consisting of a nine-layer slab in order to assure the highest quality of the structural input data for the electronic structure calculations. The goal of this paper is to determine all surface states and resonances as accurately as reasonably possible. Since their energies and spatial distribution may vary with the relaxation we had to make sure that the supercell size is large enough. This will be discussed in detail later.

Our results for the structural parameters for the InP, AlAs, and InAs(110) surfaces can be found in Table II (displacements) and in Table III (atomic distances). The results are compared with previous calculations and experiments in Table IV (atomic distances) and in Table V (bond angles and lengths). Although in general the agreement is good we want to emphasize some features.

(a) The well-known first-layer relaxation, consisting of the upward movement of the anion relative to the cation, is well reproduced in our calculation. In fact, the smallest supercell and the smallest **k** point set yield this relaxation already correctly. Our calculated relative vertical displacement $\Delta_{1,\perp}$ of the surface anion and cation corresponds within less than 5% to the LEED data. This is close to the experimental variation between different LEED results and between different calculations in the literature. The first-layer displacements are also the most accurately determined ones (experimentally within ±5 pm) and affect the electronic structure

TABLE II. III-V (110) structural relaxation: Converged results for a supercell of nine atom layers where eight layers are relaxed and the central one is kept fixed. A plane-wave cutoff of 12.25 Ry has been used. The displacements of the atoms perpendicular and parallel to the surface are expressed in units of the natural bulk distances given in the first line. The atom type is indicated in the second column. A = anion (As or P), C = cation (Al or In). The definitions of the displacements are shown in Fig. 1(a), the labels for the displacements are found in the first two columns of the table.

layer i	Atom	$\delta_\parallel$ (a_0)	$\delta_\perp$ $(a_0/\sqrt{2})$	$\delta_\parallel$ (a_0)	$\delta_\perp$ $(a_0/\sqrt{2})$	$\delta_\parallel$ (a_0)	$\delta_\perp$ $(a_0/\sqrt{2})$
		AlAs (a_0 = 5.6290 Å)		InAs (a_0 = 6.0335 Å)		InP (a_0 = 5.8549 Å)	
1	A	−0.029 025	0.067 205	−0.032 207	0.063 082	−0.029 991	0.058 064
	C	−0.073 909	−0.109 636	−0.072 149	−0.113 863	−0.069 787	−0.108 993
2	C	0.006 546	0.032 666	0.006 169	0.024 550	0.004 659	0.022 792
	A	0.004 644	0.003 574	0.004 896	−0.006 376	0.004 111	−0.006 081
3	A	−0.002 259	0.013 493	−0.001 515	0.008 814	−0.001 638	0.008 014
	C	0.001 270	0.000 160	0.000 603	−0.006 254	0.000 192	−0.006 742
4	C	0.002 252	0.005 999	0.002 204	0.004 148	0.002 075	0.003 695
	A	0.001 025	0.000 207	0.002 010	−0.002 752	0.001 991	−0.002 700

calculations the most among all relaxations.

(b) Our calculated bulk lattice constants are in all cases smaller than the experimentally determined ones. This is due to the use of the LDA, which is known to lead to overbinding. Differences among theoretical results of different groups should be due to various degrees of convergence (energy cutoffs, **k** points, slabs) of the pseudopotential calculation.

(c) As stated earlier, the most prominent structural parameter of the surface is the buckling angle ω, which has been determined by several experimental techniques. Our results agree well within about 1° with the experimental results. Only for InAs(110) the best fit of LEED experiments yielded a buckling angle of 36.5°,[79] while other fits lead to a buckling angle in the usual range around 30°.[79,80] Our calculations favor a buckling angle of about 30° also for InAs.

(d) Our calculated bond lengths change by less than 1.3%. This is not always in agreement with the existing LEED data. Although the changes have usually the same magnitude as most previous experimental results (with the exception of AlAs), they are sometimes in the opposite direction (see the $c2a1$ bond in Table V). It should be noted that theoretical results of different groups all yield similar values and the same trends of disagreement compared to the LEED data. In fact, the theoretical results favor the pure bond rotation model even more than the experiments. The degree of bond relaxation is found to be very small in theory and small but measurable in experiments. This might be a temperature effect neglected in the calculation.

(e) The relaxation is known to result in a planar threefold sp^2 configuration of the surface cation and a pyramidal sp^3-like configuration of the anion. This has been suggested as the driving force of the relaxation. Our calculation reproduces the respective configurations, as can be seen in Table III. The angles α, β, and γ are close to those of the ideal planar and pyramidal configurations.

(f) The second-layer anions and cations relax in the opposite direction compared to the surface anions and cations, respectively. The anion in the second layer relaxes downward relative to the second-layer cation. The values obtained from our calculations agree well with this trend obtained from LEED data.

(g) The lateral displacements agree, within the experimental uncertainty, with LEED measurements.

In summary, our calculations reproduce the experimental measurements of the atomic relaxation, in general, quite well. Most deviations are within the variations of the reported experimental values. Thus, the structural parameters obtained with the supercell consisting of nine layers should be sufficiently accurate for further detailed analyses of the electronic structure.

TABLE III. III-V (110) structural relaxation: Converged results for a supercell of nine atom layers. A plane-wave cutoff of 12.25 Ry has been used. The distances of atoms inside one layer and between successive layer are expressed in units of the natural bulk distances given in the first line. The definitions of the distances are shown in Fig. 1(b), the layer index is found in the first column of the table.

Layer i	$\Delta_{i,\perp}$ $(a_0/\sqrt{2})$	$\Delta_{i,x}$ $(3/4a_0)$	$d_{i,i+1,\perp}$ $(1/2a_0/\sqrt{2})$	$d_{i,i+1,x}$ $(1/2a_0)$
		AlAs (a_0 = 5.6290 Å)		
1	0.176 843	1.059 845	0.715 392	1.160 910
2	0.029 093	0.997 464	0.980 162	1.010 551
3	0.013 333	0.995 294	0.988 321	1.001 963
4	0.005 792	0.998 364	1.000 414	1.004 504
		InAs (a_0 = 6.0335 Å)		
1	0.176 945	1.053 256	0.723 173	1.156 636
2	0.030 926	0.998 302	0.969 619	1.011 132
3	0.015 069	0.997 176	0.979 196	1.003 202
4	0.006 900	0.999 741	0.994 497	1.004 409
		InP (a_0 = 5.8549 Å)		
1	0.167 057	1.053 060	0.736 431	1.148 891
2	0.028 873	0.999 270	0.971 811	1.008 934
3	0.014 756	0.997 559	0.979 126	1.003 765
4	0.006 395	0.999 889	0.994 600	1.004 149

V. ELECTRONIC STRUCTURE OF THE SURFACE

Close to a surface at least three types of electron states exist: bulk states distributed over the entire crystal (in our

TABLE IV. Comparison of distances of surface atoms in different III-V compounds according to the definitions in Fig. 1(b). The distances are expressed in units of the respective bulk distances given in the first line. The upper sections of the entries for each material are experimental results from LEED measurements, the lower sections are theoretical results, including this work.

III-V Bulk	Ref.	a_0 (Å)	$\Delta_{1,\perp}$ $(a_0/\sqrt{2})$ 0.0000	$\Delta_{1,x}$ $(3/4a_0)$ 1.0000	$d_{12,\perp}$ $(1/2a_0/\sqrt{2})$ 1.0000	$d_{12,x}$ $(1/2a_0)$ 1.0000	$\Delta_{2,\perp}$ $(a_0/\sqrt{2})$ 0.0000	$\Delta_{2,x}$ $(3/4a_0)$ 1.0000
InAs	67	6.0585	0.182	1.097	0.706	1.188	0.033	
	13	6.0585	0.184	1.055	0.622	1.116		
	this work, 12.25 Ry	6.0335	0.176	1.052	0.727	1.153	0.029	0.998
	this work, 20.25 Ry	6.0126	0.174	1.051	0.739	1.161	0.022	0.996
	35, 18 Ry	5.861	0.181	1.061	0.697	1.159	0.031	
InP	67	5.8695	0.166	1.041	0.663	1.177	0.034	
	22	5.8695	0.157	1.041	0.740	1.136	0.027	
	13	5.8695	0.195	1.034	0.624	1.119		
	this work, 12.25 Ry	5.8549	0.166	1.053	0.740	1.149	0.027	0.999
	35, 18 Ry	5.662	0.167	1.064	0.717	1.136	0.029	
AlAs	67	5.66	0.162	1.038	0.665	1.173	0.030	
	this work, 12.25 Ry	5.6290	0.176	1.059	0.718	1.161	0.028	0.997

calculations: slab), localized surface states with an energy outside of the projected bulk bands having a high probability density at the surface, and surface resonances having a high probability density at the surface, but an energy within projected bulk bands. The surface resonances are slowly decaying Bloch waves inside of the bulk and have an exponential decay into the vacuum, while the localized surface states decay exponentially into the bulk and the vacuum. The electronic properties of the surfaces are to a large degree influenced by the surface states (localized and resonant) and thus we will focus on them. Most previous investigations only report the localized surface states. However, the importance of resonances for the understanding of surface sensitive measurements has been demonstrated recently.[37] In this paper we will analyze localized surface states and resonances in detail to obtain a complete picture of the electronic properties of the surface.

A. Band structure: overview over the existing surface states and resonances

The calculated band structure for the 17-layer slab is shown superimposed on the projected bulk band structure in Fig. 2 for InP for which we have made the most detailed analysis. For InAs and AlAs the projected bulk density of states is calculated in the same way as for InP, but the electronic structure has only been calculated for the nine-layer slab, which we have used for the calculation of the atomic

TABLE V. Comparison of relaxation angles and bond length changes. The organization of the table is the same as in Table IV. $\delta c_i a_j$ are the changes of the bond lengths between the cation of the ith layer and the anion of the jth layer relative to the cation anion bulk bond length.

III-V Bulk	Ref.	ω (deg) 0.0	α (deg) 109.5	β (deg) 109.5	γ (deg) 109.5	$\delta c_1 a_1$ (%) 0.00	$\delta c_2 a_1$ (%) 0.00	$\delta c_1 a_2$ (%) 0.00
InAs	67	31.0	87.5	116.4	121.8	−3.9	2.1	1.4
	13	32.0	91.0	110.3	124.8	−0.5	−2.8	
	This work, 12.25 Ry	30.6	89.1	110.7	124.3	−0.74	0.63	−0.95
	This work, 20.25 Ry	30.2	89.0	110.5	124.3	−0.65	0.92	−0.91
	35, 18 Ry	32.0	88.9	111.4	123.9	−1.18	−0.18	−1.82
InP	67	28.1	90.3	109.7	124.8	−0.2	−7.4	−1.7
	22	26.5	91.7	110.4	123.8	−0.6	−1.0	−2.1
	13	31.8	89.7	106.6	126.6	1.8	−3.3	
	This work, 12.25 Ry	29.2	90.2	111.4	123.7	−1.18	0.58	−1.02
	35, 18 Ry	30.1	90.4	112.5	123.2	−1.78	−0.23	−1.89
AlAs	67	27.3	90.8	109.5	124.9	−0.04	−7.84	−2.29
	This work, 12.25 Ry	31.2	89.0	111.6	123.9	−1.29	0.38	−1.30

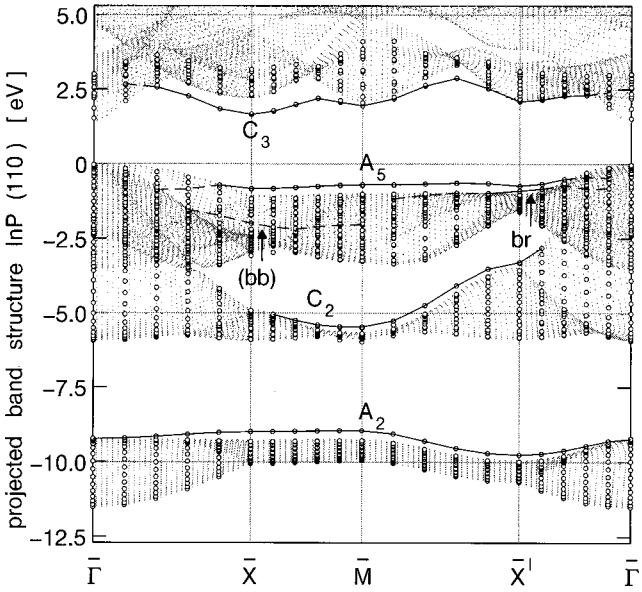

FIG. 2. Band structure of the buckled InP(110) surface along high-symmetry lines of the surface Brillouin zone, calculated with a slab consisting of 17 atom layers and a vacuum equivalent to seven atom layers. Energies are measured relative to the valence-band maximum. The shaded area shows the band structure of bulk InP projected to the (110) surface. The open dots are the eigenvalues calculated for the surface supercell. Eigenvalues in the conduction band have been rigidly shifted by 0.573 eV to reproduce the experimental bulk band gap of InP ($E_{g,\mathrm{th}}=0.847$ eV; $E_{g,\mathrm{exp}}=1.42$ eV). The identified localized and resonant states are shown as solid and dashed lines, respectively. A_2 is the localized state at the P anion; C_2 is the localized state at the In cation; bb is the resonant states with anion backbond character; A_5 is the localized anion dangling bond (db); br is the localized (at $\bar{X}'$) and resonant bridgebond state; C_3 is the localized dangling bond state at the cation with p_z character.

relaxation of the (110) surface (see above). This allows a qualitative comparison but no quantitative analysis. The states, whose eigenvalues are in the band gaps or in the pocket gap are localized surface states. As can be seen in Fig. 2, close to the center of the Brillouin zone these bands dip into the bulk bands and thus the corresponding states become surface resonances. Some surface induced features have eigenvalues inside the projected bulk bands for all $\mathbf{k}_\parallel$ vectors; they are pure resonances. Following the notation of Ref. 29, the surface states are labeled A_i and C_i according to their localization close to anions and cations, respectively. The states are numbered from the lowest one upward. The following characteristics can be deduced.

(a) The surface band structures of the different materials are qualitatively similar. The same type of states exist for all compounds calculated.[69]

(b) As usual the band gaps obtained by the local-density approximation are too small. They need to be corrected for quasiparticle effects.[34] We corrected this by rigidly shifting all empty (conduction-band) states upward until the correct experimentally measured bulk band gap is obtained at the $\bar{\Gamma}$ point. The necessary shifts are 0.41, 0.573, and 0.996 eV for InAs, InP, and AlAs, respectively. This applies to the bulk and the surface slab calculations in the same way. The experience of other authors[81,82] shows that this ''scissors'' procedure works with an accuracy of about 0.2 eV.

(c) Only surface resonances, but no localized surface states, exist at the $\bar{\Gamma}$ point of the surface Brillouin zone. Localized surface states can, e.g., be found at the boundary of the Brillouin zone ($\bar{M}$, $\bar{X}$, and $\bar{X}'$ points).

(d) The dispersion of the localized states and resonances agree well with the dispersion measured by photoemission. We can correlate all experimentally observed surface features with those obtained theoretically. In particular, the dispersion of the occupied dangling bond state (uppermost occupied state) agrees well with the dispersion found in angle-resolved photoemission experiments.[18,19,83,84] The dispersion of the lowest empty surface state agrees also with inverse photoemission results.[85–87]

(e) Our results are in qualitative and partly quantitative agreement with other theoretical findings. However, most of the earlier calculations used semiempirical pseudopotentials,[29–31] experimentally determined relaxation data,[31] and/or the X_α approximation for the exchange correlation term. Our calculations are in fact only comparable to a very limited set of earlier calculations.[33–36,88] Of those, Zhang and Cohen[33] and Qian, Martin, and Chadi[88] used a very narrow vacuum region of four and three layers, respectively, to describe the vacuum barrier. Our analysis shows that surface electron states decay over about 2.5 layers into the vacuum (see below). Thus, in these early calculations the wave functions overlap and surface interactions perturb the results. The resulting wave functions cannot be used for the simulation of STM images. Alves, Hebenstreit, and Scheffler[35] performed calculations very similar to ours. The main difference is the missing analysis of the surface resonances. In addition, their supercell of eight layers (compared to 17 in our electronic structure calculations) is too small for the determination of the exact contributions of surface resonances. Their analysis of the distribution of localized states/resonances is incomplete for the understanding of voltage-dependent STM images (and partly for photoemission data, too), since only the dangling bond states above the anion and cation with energies close to the band gap were taken into account. The early calculation of Zunger[30] includes surface resonances. However, the detailed analysis of the spatial distribution of the states, particularly the extension into the vacuum, is missing.

In conclusion, a comparison with the experiments and theoretical calculations reported in the literature demonstrates that our calculations yield the electronic structure of the surface accurately. This gives a solid basis for the analysis of the character and properties of each surface state (localized or resonant) and for the determination of the contribution of these states to STM images.

B. Localization and decay of the surface states into the vacuum

Figure 3 shows a comparison of the DOS of bulk InP (dotted line) and of the InP(110) surface supercell (dashed line) as a function of energy. Figure 3(a) is the overview, while Figs. 3(b), 3(c), and 3(d) are expansions of the energy scale of Fig. 3(a). The solid line shows the LDOS integrated over a (110) plane at a distance of 4.378 a.u. above the

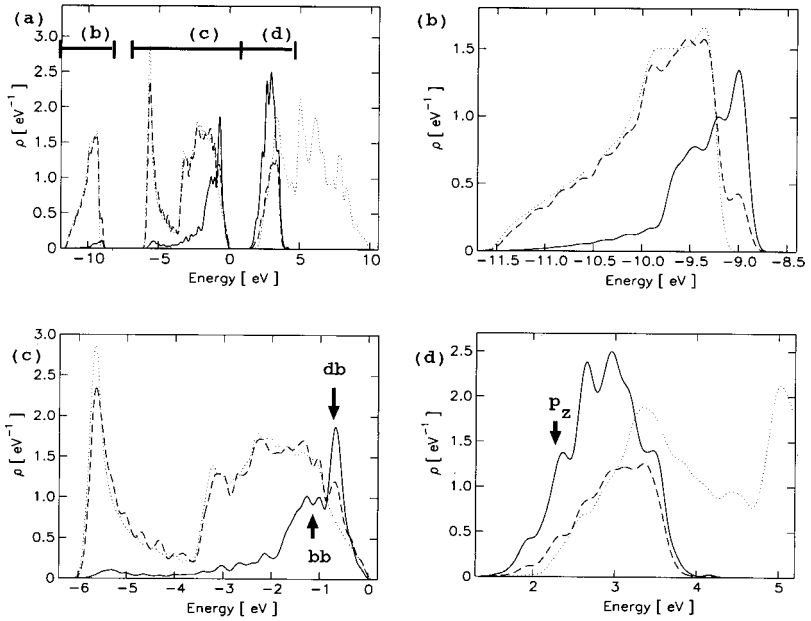

FIG. 3. Comparison of the DOS for InP. (a) Total DOS of bulk InP (dotted), DOS of InP in the surface supercell (dashed), and local DOS, integrated over the plane at $d=4.378$ a.u. above the surface anion (solid line). The surface DOS and LDOS are meaningful up to 3 eV above the minimum of the conduction band only (see text). The bulk DOS is normalized to eight electrons, contained in the occupied states. For the surface DOS and LDOS arbitrary units are used. (b)–(d) show expansions of the energy scale of the sections indicated in panel (a). The pronounced contributions of the localized surface states are indicated (db, bb, p_z).

outermost surface anion in the vacuum (this ''surface LDOS'' is shown on a different scale). We have calculated only a limited number of unoccupied eigenstates and eigenvalues for the surface supercell. Thus the DOS and LDOS of the surface are complete only up to 3 eV above the conduction-band minimum. The energy distribution of the surface LDOS deviates strongly from the bulk DOS; only those states contribute that decay particularly slowly into the vacuum. The surface-specific contributions are from localized surface states and resonances. They can especially be found for energies close to the band edges. However, no states are found within the fundamental band gap. The most important features are labeled db (occupied dangling bond), bb (occupied backbond), and p_z (empty dangling bond with p_z character). These features correspond to the states labeled A_5, A_4, and C_3, respectively, according to the conventional notation. C_4 corresponds to a group of resonances above the C_3 state. In the following we will, however, keep the character of the state as the name. The occupied dangling bond appears as a very sharp peak and indeed it is a localized surface state for most **k** points, whereas the backbond appearing as a broad feature is a surface resonance. The empty dangling bond also is a well-localized surface state. Its contribution to the surface LDOS is, however, very small and nearly disappears in the large number of empty resonances with a large LDOS. These empty resonances consist of a large variety of different states. We have analyzed the spatial distribution (vertical to the surface as well as lateral) of all states with energies close to the fundamental gap. The identification of the characters of each surface feature will follow below.

Comparing the surface LDOS with the DOS of the supercell or the bulk one finds an exponential damping of the LDOS contributions with decreasing energy. This is understood by the fact that wave functions of electrons bound to the crystal (i.e., with energy eigenvalues ϵ below the vacuum zero) have an exponential decay into the vacuum ($z>0$): $\Psi(z)\sim e^{-\kappa z}$, where the decay constant $\kappa\sim(2m|\epsilon|/\hbar^2)^{1/2}$ and ϵ is measured from the vacuum zero.

The surface LDOS in Fig. 3 has been calculated for a fixed distance of 4.378 a.u. above the outermost anion (averaging over a layer 0.43 a.u. wide). The distance dependence of the surface LDOS is demonstrated in Fig. 4. Figure 4 shows that with increasing distance d the absolute magnitude of the LDOS decreases exponentially. However, due to the fact that the decay constant κ depends on energy, the LDOS of the empty states gains relative weight with increasing separation from the surface. Obviously the empty surface states decay slower into the vacuum. All occupied states can be identified well for all three distances shown. The empty dangling bond (p_z) disappears with increasing distances in the noise of the empty resonances. It is necessary to investigate the decay characteristics of each surface feature in more detail.

1. Occupied states

We have found three distinct types of occupied surface states: dangling bond states at the anion, backbond states (bb) establishing the bonds of the surface anion with the cation in the second layer, and bridgebond states establishing the bonds between the surface anion and cation. The distinction between db, bb, and br states can be demonstrated most clearly for the states at the X' point. Typical examples of the charge-density distribution are shown in Figs. 5–7, respectively. The following characteristics can be deduced.

(1) The dangling bonds and backbonds show two lobes, one directed toward the vacuum side and one toward the

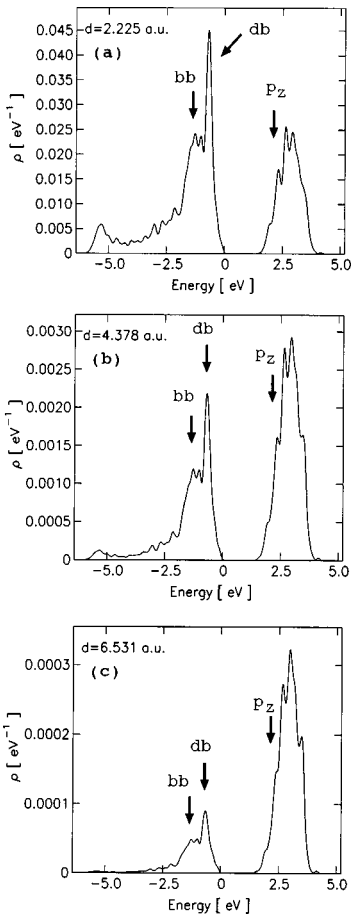

FIG. 4. The LDOS of InP (110) integrated over planes at different distances d above the surface anion as indicated in the panels. The occupied localized (db) and resonant (bb) states are easily recognized while the unoccupied localized (p_z) state is barely visible. At the largest distance the energy dependence of the decay length can be seen most pronouncedly: The relative magnitude of the LDOS increases exponentially with increasing energy.

subsurface layers. The lobes on the vacuum side are shifted (relative to the anion position) in [001] and [001] directions for the backbond and dangling bond, respectively. The db state is localized. The bb state is a resonance. The bulk side lobe of the backbond is directed toward the cation in the second surface layer. The dangling bond lobe oriented into the bulk lies inside a tetraeder consisting of two surface cations, one surface anion, and one second-layer cation. (2) The bridge bond is localized along the bonds between the surface anion and cation. It is a localized state at the $\bar{X}'$ point. There are two maxima of the bridgebond state per unit cell. (3) For a general $\mathbf{k}_\parallel$ point a clear distinction between the db, bb, and br states cannot be made, because a number of ''mixed states'' occur. In fact, the typical resonance is usually a mixed state, even if one type of character may dominate. (4) The dangling bond state is a localized surface state for $\mathbf{k}_\parallel$ points in a large part of the Brillouin zone. We find the bridgebond to be a true localized state only very close to the $\bar{X}'$ point. All other features are surface resonances.

The decay into the vacuum and into the bulk of all three types of states is shown in Fig. 8 for two $\mathbf{k}_\parallel$ points ($\bar{X}'$ point and $\mathbf{k}=0.3\mathbf{k}_{[10]}+0.4\mathbf{k}_{[01]}$). The dangling bond and the

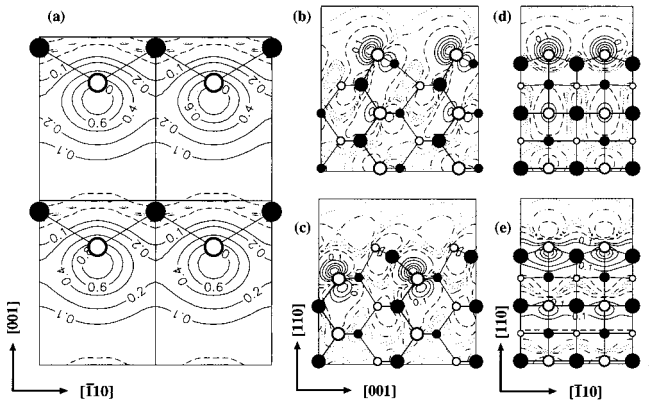

FIG. 5. The localized occupied dangling bond state A_5 at $\bar{X}'$. Shown are cuts of $|\Psi(\vec{r})|^2$ in different planes: (a) (110) plane at $d=4.378$ a.u. above the surface anion; (b),(c) (110) planes through the anion and cation, respectively; (d),(e) (001) planes displaced along [001] from the surface anion by $-0.094a_0$ and $+0.114a_0$, respectively. The circles denote the sites of anions (empty) and cations (full) projected to the respective plane shown. The numbers at the contour lines are fractions of the maximal probability density for the state in that particular plane.

bridgebond decay very fast into the bulk at the $\bar{X}'$ point [Fig. 8(a)]. Therefore, the overlap of the wave functions localized at the two surfaces of the slab is small and consequently the symmetric and antisymmetric combination of the states (which are eigenfunctions for the mirror symmetry of our slab) exhibit only a very small splitting (0.7 and 0.3 meV). The backbond state decays much slower into the bulk and the overlap is not negligible; even for the largest slab of 17 layers the splitting is 130 meV. This demonstrates that we indeed need such a large supercell to obtain reliable energy values. The decay at the second $\mathbf{k}_\parallel$ point has similar characteristics but the decay into the bulk is slower. Again the dangling bond decays faster into the bulk than the resonances. The splitting observed here was 6.9 and 176 meV for the dangling and backbond, respectively. The splitting is larger than that for the $\bar{X}$ point.

All states decay much faster into the vacuum than into the bulk. However, distinct differences of the decay lengths and the amplitudes can be observed between different states. The decay of the dangling bonds and backbonds is nearly equal

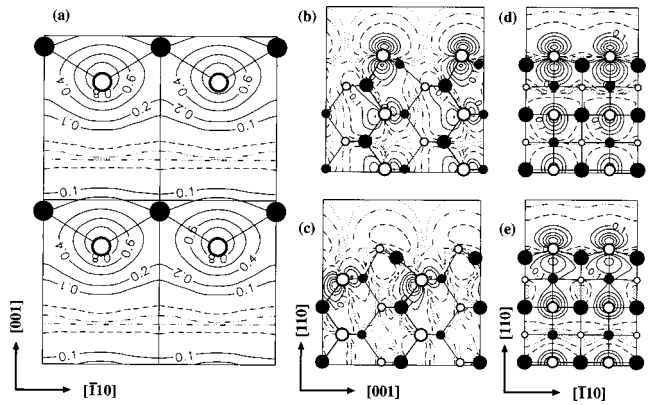

FIG. 6. The resonant occupied backbond state (bb) at $\bar{X}'$. Shown are cuts of $|\Psi(\vec{r})|^2$ in the same planes as Fig. 5.

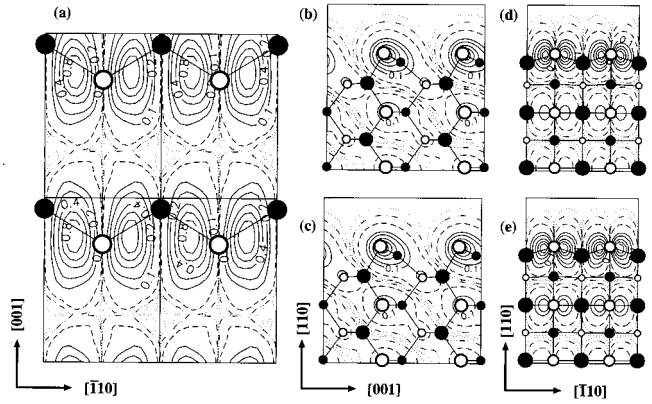

FIG. 7. The localized occupied bridgebond state (br) at $\overline{X'}$. Shown are cuts of $|\Psi(\vec{r})|^2$ in different planes: (a),(d),(e) same as Fig. 5; (b),(c) (110) planes on either side of the anion exactly between the anion and cation.

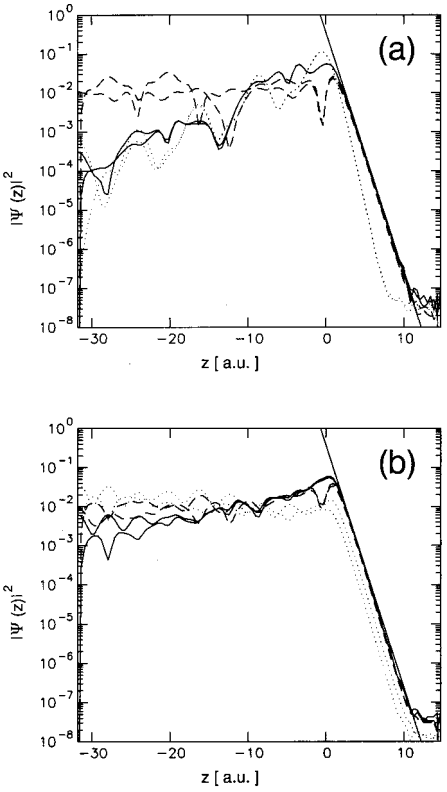

FIG. 8. Decay of occupied states into the bulk ($z<0$) and vacuum ($z>0$). Shown is $|\Psi(z)|^2$ (log scale), i.e., the probability distribution integrated over planes parallel to the (110) surface, as a function of the distance z from the surface (at $z=0$). (a) shows db (solid lines), bb (dashed lines), and br (dotted lines) states at $\overline{X'}$. (b) shows db (solid lines), bb (dashed), and bulk (dotted) states at $\vec{k}=0.3\vec{k}_{[10]}+0.4\vec{k}_{[01]}$. The straight line indicates the exponential decay of the db states with decay length $\lambda=0.7$ a.u. The br states in (a) have a small contribution in the vacuum, because they have a larger $\vec{k}_{\|}$ and thus a smaller decay length, and the bulk states in (b) have a smaller amplitude at the surface.

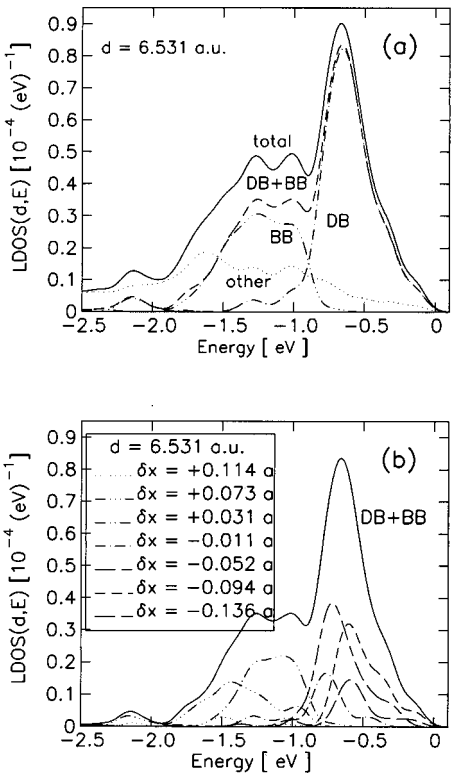

FIG. 9. The LDOS for InP(110) integrated over a plane at $d=6.531$ a.u. above the surface anion for the occupied surface states (energies in the valence band). (a) The LDOS sorted according to the bond character: total, all states; DB, dangling bonds; BB, back bonds; DB+BB, sum of both; other, other character. (b) The LDOS of db and bb states sorted according to the position δx of the maximum of the probability density of the state in the plane considered. δx is the distance along [001] measured from the position of the surface anion. The energy of the state and the db character increase when the maximum moves in the [001] direction, i.e., with decreasing δx.

(in decay length and amplitude) and it is the slowest of all occupied states. Their density is, at large distances, about one (to two) orders of magnitude larger than that of all other states. The bridgebond state decays faster than typical bulk states [see Fig. 8(a)]. The very short decay length is due to the higher spatial frequency (half the unit cell) of the bridgebond state. Depending on the distance range their density may be even smaller than that of bulk states. Bulk states have about the same decay length as the dangling bonds and backbonds, but a smaller amplitude [see Fig. 8(b)].

The decay into the vacuum indicates already that typical STM images can only image dangling bond and backbond states, but not bulk or bridgebond states as proposed previously.[89,90] Only under special conditions, such as very small separations like those occurring during the spectroscopy in and close to the band gap[91,92] or during scanning at very low magnitudes of voltages,[93] a small contribution of bulk and other states may be possible. In any STM image acquired under standard conditions, however, dangling bonds and backbonds dominate the contrast.

Figure 8 demonstrates the necessity for a large vacuum layer in the slab. We have followed the decay of the states down to the level of numerical noise. We have reached the

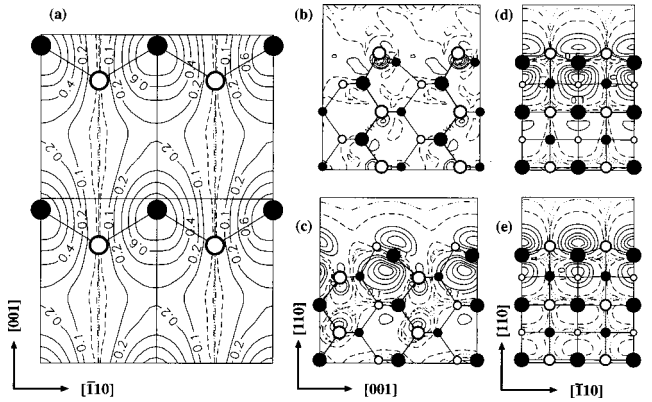

FIG. 10. The localized unoccupied C_3 state (p_z character) at $\bar{X}$. Shown are cuts of $|\Psi(\vec{r})|^2$ in different planes: (a),(b),(c) same as Fig. 5; (d),(e) (001) planes displaced along [001] from the surface cation by $-0.058a_0$ and $+0.109a_0$, respectively. The numbers at the contour lines are fractions of the maximal probability density for the state in that particular plane.

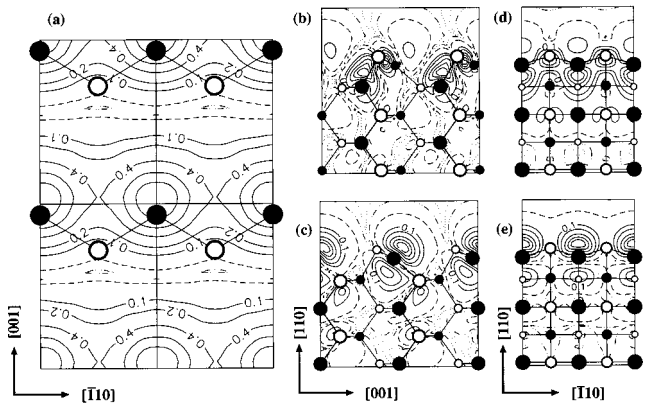

FIG. 11. A resonant unoccupied ''hybrid'' state at $\vec{k}=0.2\vec{k}_{[10]}+0.5\vec{k}_{[01]}$ with contributions at the anion and cation. Shown are cuts of $|\Psi(\vec{r})|^2$ in different planes: (a),(b),(c) same as Fig. 5; (d),(e) (001) planes displaced along [001] from the surface anion by $+0.073a_0$ and from the cation by $+0.067a_0$, respectively. The state shows pronounced p_z character at the surface cation.

asymptotic behavior relevant for comparison with STM experiments.

The dispersion of the different states includes important information for the detailed interpretation of spectroscopic measurements, such as scanning tunneling spectroscopy. Figure 9(a) shows an analysis of the relative contributions of dangling bond and backbond states as a function of energy. This analysis has been performed at a distance of 6.531 a.u. from the surface. The occupied dangling bond appears as a sharp and well-localized surface band. It has its maximum at -0.66 eV and ranges from approximately -0.4 to -0.9 eV below the valence-band maximum (VBM). The backbond appears as a broad resonance with two maxima at -1 and -1.25 eV below the valence-band maximum. It ranges from about -0.9 to -1.6 eV.

Depending on the bond character, different surface states have different lateral probability distributions $|\Psi(r_\parallel)|^2$. The backbonds and dangling bonds have both lobes pointing into the vacuum, but into different directions. This suggests that the lateral position $r_{\parallel,0}(\epsilon)$ of the maximum of the density of states in the vacuum $|\Psi(r_{\parallel,0})|^2$ depends on the character of the surface state (db or bb) and thus varies with the energy ϵ. Figure 9(b) shows the LDOS accumulated for states that have their maximum of the lateral distribution probability at $r_{\parallel,0}=(\delta x,0)$ (positive δx correspond to a shift in [001] direction in the (x,y) plane of the surface unit cell). The results show that the maximum of the density of states is shifted in [001] direction relative to the surface anion, when the energy of the occupied states rises from -2 to -0.5 eV. With the knowledge of Fig. 9(a) we can conclude that the dangling bond and backbond contributions to the density of states in the vacuum are shifted laterally in [001] and [001] directions relative to the anion, respectively.

2. Empty states

The empty states cannot be separated into different types of states as easily as the occupied ones. We found a large variety of different states, which all have a similar extension or decay into the vacuum. There are states localized at the cation, anion, and above both types of atoms. Figures 10–13 show four states of those: a p_z-like state or dangling bond localized at the cation, a mixed state, another state having a noticeable density above the surface anion and cation, and a state with two maxima per unit cell, respectively. Each of the examples stands for a group of states. The p_z-like state is a sharp surface state at the $\bar{X}$ and $\bar{M}$ points. It appears as a row along the [001] direction (Fig. 10). Its minimum is about 1.7 eV above the VBM (see Fig. 2, C_3). The mixed state is a hybrid state mostly localized above the cation (Fig. 11). It is 2.34 eV above the VBM. There are many other states with similar features. All of them appear as a row along the [110] direction. The state in Fig. 12 has a higher density of states above the anion compared to the cation. We observed a variety of such states. In fact a partial localization of empty states at anions was also found by Tersoff and Hamann.[70] We also observed a group of states with two maxima in the surface unit cell.

Figure 14 shows the decay of these states into the vacuum. The straight line is the decay of the occupied dangling bond. All empty states decay slower than the occupied ones. This is a direct consequence of the energy dependence

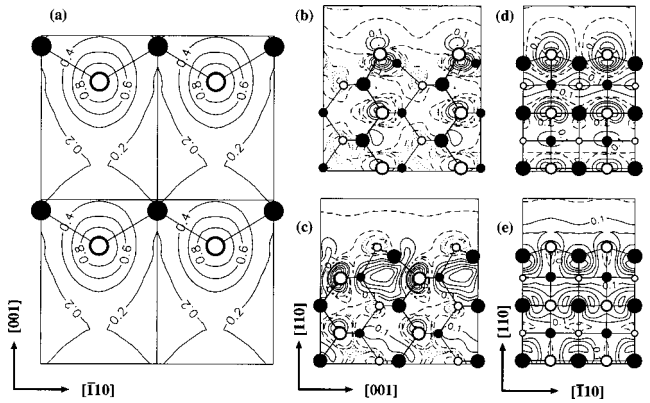

FIG. 12. A resonant unoccupied hybrid state at $\vec{k}=0.2\vec{k}_{[10]}$. Shown are cuts of $|\Psi(\vec{r})|^2$ in different planes: (a),(b),(c) same as Fig. 5; (d),(e) (001) planes displaced along [001] from the surface anion by $-0.01a_0$ and from the cation by $+0.109a_0$, respectively. The state shows some db character at the surface anion.

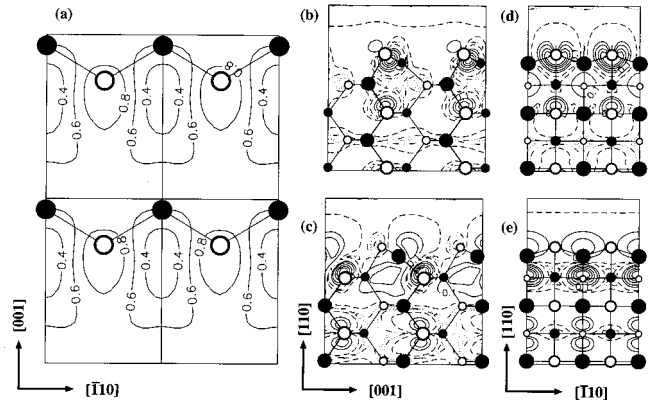

FIG. 13. A resonant unoccupied hybrid state at $\vec{k}=0.2\vec{k}_{[10]}$. Shown are cuts of $|\Psi(\vec{r})|^2$ in different planes: (a),(b),(c) same as Fig. 5; (d),(e) (001) planes displaced along [001] from the surface anion by $+0.031a_0$ and from the cation by $+0.234a_0$, respectively. The state has several maxima in the (110) plane.

of the decay constant $\kappa(\epsilon)$ discussed above. Furthermore, the empty resonances decay slower than the p_z-like state. Figure 15 shows the energy distribution of the empty states at a distance of 6.531 a.u. above the surface. The states have been distinguished according to their localization above the anion and cation. The figure demonstrates that the unoccupied states localized above the cation are lower in energy than the states with their maxima above the surface anion.

VI. COMPARISON WITH SCANNING TUNNELING MICROSCOPY IMAGES

In this section we compare the theoretical results with the STM images measured on the (110) cleavage surfaces of the different III-V compound semiconductors. We first characterize the theoretical STM images and discuss the contributions of different states. Finally we compare these results with the experimental data.

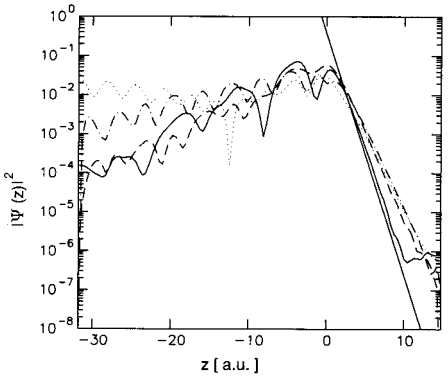

FIG. 14. Decay of unoccupied states into the bulk ($z<0$) and vacuum ($z>0$). Shown is $|\Psi(z)|^2$ (log scale), i.e., the probability distribution integrated over planes parallel to the (110) surface, as a function of the distance z from the surface (at $z=0$). The states are characterized by having a maximum at the cation (p_z dangling bond, solid line; hybrid state, dash-dotted line), or at the anion (hybrid states, dashed and dotted lines). The straight line indicates the exponential decay of the occupied db states with decay length $\lambda=0.7$ a.u. All states have a large contribution in the vacuum but the energy of the ''anion maximum'' states is deeper in the conduction band (see Fig. 15).

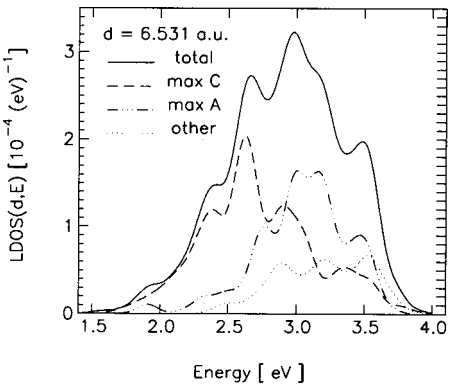

FIG. 15. The LDOS of InP(110) integrated over a plane at $d=6.531$ a.u. above the surface anion for the unoccupied surface states (energies in the conduction band) sorted according to bond character: total, all states; max *C*, maximum at cation; max *A*, maximum at anion; other, other character. The states with a maximum at the anion have higher energies.

A. States contributing to STM images

The STM images are acquired with tip-sample separations of typically 0.5 nm or more.[94] Only in a few cases could this separation be reduced further,[93] but tip effects became dominant.[95] We do not want to focus on such tunneling conditions, but rather focus on the conventional separations, where the assumption of no tip effect is valid. The rather large tip-sample separation requires that we analyze the LDOS far in the vacuum. Only states decaying slowly can contribute to the STM images. As shown above, these states are the occupied dangling bonds (A_5) and backbonds (A_4), as well as the empty dangling bond (C_3: p_z-like state) and several empty resonances (C_4). At low negative voltages only the occupied dangling bond state can contribute to the STM images. Increasing the magnitude of the voltage to such an extent that electrons from states with energies -0.9 eV can tunnel, the backbond state contributes to the occupied-state STM images, too. According to our analysis, the bridgebond decays too fast to affect the STM images. Thus, two types of occupied states contribute to the STM images.

For the empty states the situation is somewhat more complicated. The empty dangling bond contributes, but it dominates the STM images only at small voltages, since it has a rather small weight in the vacuum. The major contributions at higher voltages are from surface resonances which are anion-cation-hybrid states and thus have contributions above the anion and the cation. However, the component of the LDOS localized above the anion decays faster than that above the cation. Thus, asymptotically only the cation contribution can be measured.

B. Distance dependence of the lateral distribution of the local density of states

Figures 16, 17, and 18 show the simulated lateral distribution of the energy-integrated LDOS for different energy intervals at three different distances from the surface, i.e.,

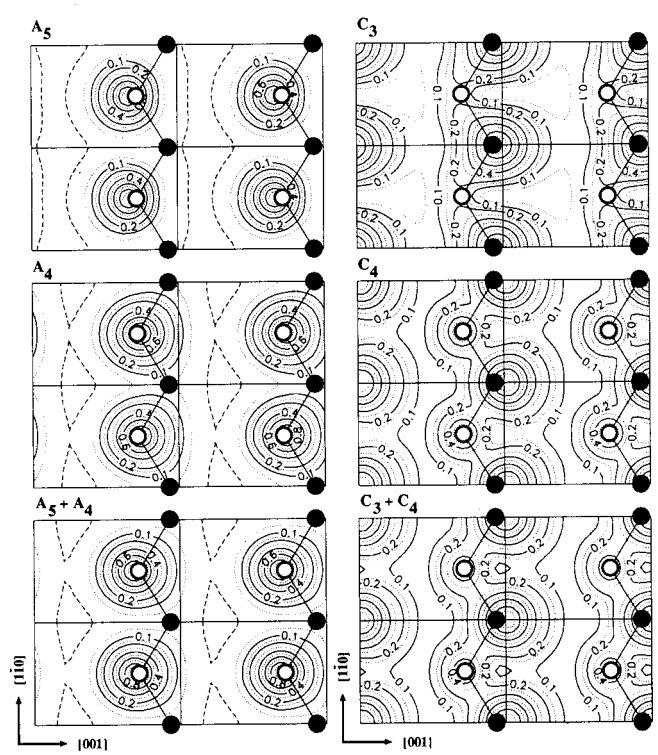

FIG. 16. Simulated STM images of the InP(110) surface at a distance $d=2.23$ a.u. above the surface anion. The energy-integrated LDOS is shown for different energy intervals. A_5, VBM to VBM-0.9 eV (range of the occupied db states); A_4, VBM-0.9 eV to VBM-1.5 eV (range of the occupied bb states); A_5+A_4, VBM to VBM-1.5 eV (range of the occupied db plus bb states); C_3, VBM to VBM$+2.2$ eV (range of the unoccupied p_z states); C_4, VBM$+2.2$ eV to VBM$+2.8$ eV (range of the unoccupied resonant hybrid states); C_3+C_4, VBM to VBM$+2.8$ eV (range of the unoccupied p_z plus hybrid states). At small distances the occupied states show a very pronounced maximum at the surface anion at all voltages. The unoccupied hybrid states show a zigzag characteristic with maxima at the cation and (smaller ones) at the anions.

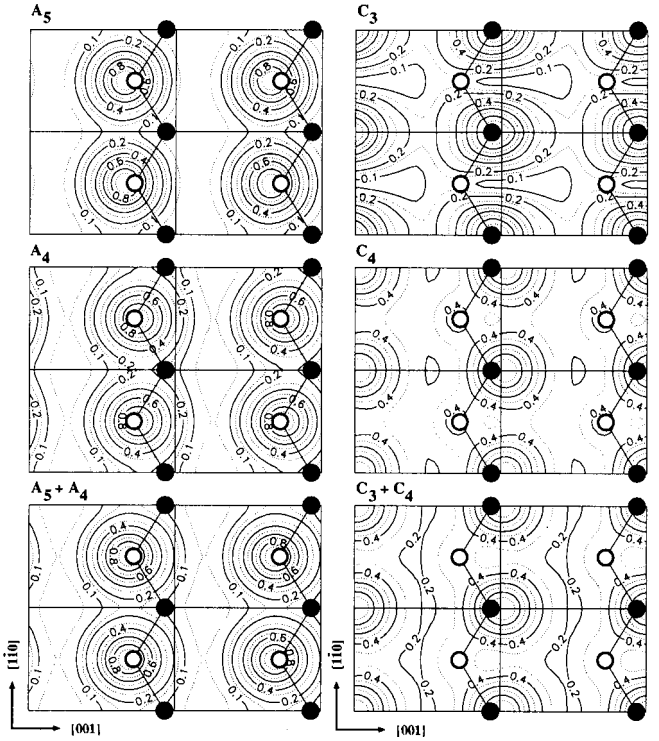

FIG. 17. Simulated STM images of the InP(110) surface at a distance $d=4.38$ a.u. above the surface anion. The different panels have the same meaning as in Fig. 16. The appearance of the occupied states has not changed much compared to shorter distances. The zigzag characteristic of the unoccupied hybrid states has decreased because the maxima at the anions are less pronounced.

2.23, 4.38, and 6.53 a.u., respectively. The frames denoted A_5 in each figure show the occupied dangling bond (energy interval VBM to VBM-0.9 eV). A_4 is the backbond (VBM-0.9 eV to VBM-1.5 eV) and A_4+A_5 is the sum of both states (VBM to VBM-1.5 eV). Similarly, the right column shows the empty states. Panel C_3 represents the empty dangling bond (VBM to VBM$+2.2$ eV), panel C_4 part of the empty resonances (VBM$+2.2$ eV to VBM$+2.8$ eV), and C_3+C_4 the sum of both empty states. It is clearly visible that the lateral distribution of the occupied states does not change much as a function of distance from the surface. The backbond (A_4) is localized nearly at the same place as the dangling bond (A_5). No large shifts occur if both states are added. In contrast, the morphology of the empty states changes drastically with distance and energy. The empty dangling bond (C_3) appears as a row along the [001] direction. The larger the distance the less corrugation it shows along that direction. The resonances (C_4) have a large LDOS above the cation and anion. At small separations they appear as zigzag chains connecting cations and anions. With increasing distance the LDOS above the anion decays faster and rows in the [110] become apparent. This means a rotation of the apparent row direction by 90° compared to the orientation of the dangling bond. Since the LDOS of the resonances is larger than that of the dangling bond, the images at higher voltages (energies) are dominated by the resonances.

C. Theoretical corrugation

We also computed from the lateral LDOS distribution the theoretical corrugations. Figure 19 shows the ratio of the corrugation along the [110] and [001] directions for the occupied in the upper frame and empty states in the lower frame. At an energy of about -0.7 eV below the VBM there is a sharp increase of the corrugation ratio of the occupied states at all distances due to the contribution of the localized anion db state, which shows little dispersion at the edges of the surface Brillouin zone (Fig. 2). The step becomes more pronounced with increasing distance because the relative contribution of the db state increases with distance (see the decay in Fig. 8 and the peak to valley ratios in Figs. 16–18).

For the empty states the corrugation ratio decreases steadily with energy above the CBM at all distances. According to our analysis many states with a broad dispersion contribute. Only for the larger distances a change of the predominant row orientation from [001] rows (corrugation ratio >1) to [110] oriented rows (corrugation ratio <1) can be expected at an energy of VBM$+2.3$ eV.

D. Experimental STM images

Figure 20 shows the experimentally measured constant current STM images for different voltages for GaP and

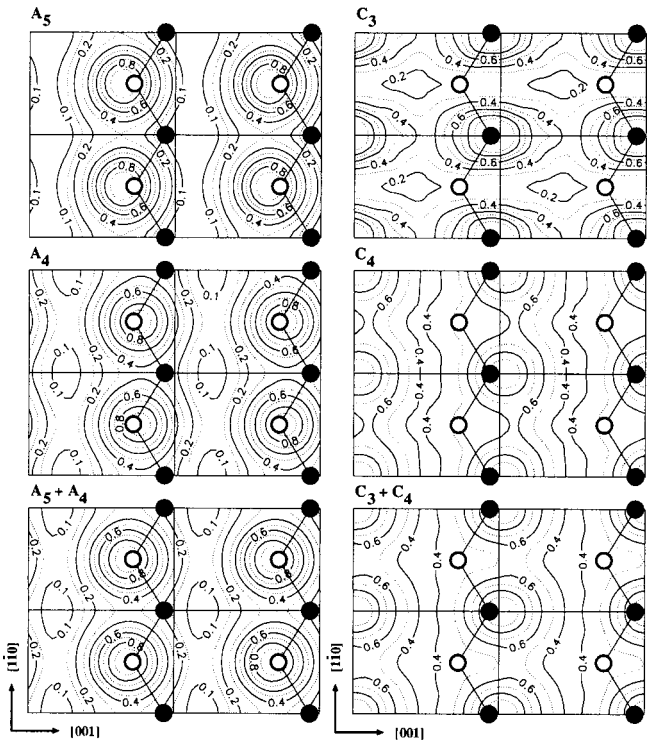

FIG. 18. Simulated STM images of the InP(110) surface at a distance $d=6.53$ a.u. above the surface anion. The different panels have the same meaning as in Fig. 16. The appearance of the occupied states is still the same as at shorter distances, only the corrugation has decreased. The zigzag characteristic of the unoccupied hybrid states is gone. Instead, the high-voltage (VBM+2.8 eV) STM image shows cation rows along the [110] direction, whereas at lower voltage (VBM+2.2 eV) the rows appear in the [001] direction.

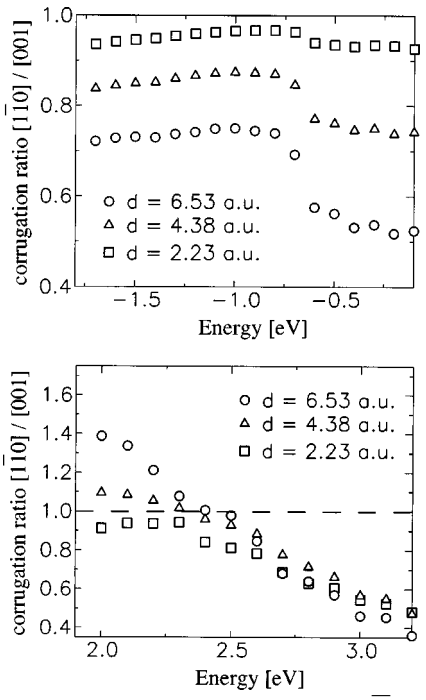

FIG. 19. Calculated corrugation ratios in the $[\bar{1}10]$ direction and in the [001] direction as a function of the energy relative to the VBM for three distances d from the surface anion. For negative energies (occupied states images, upper panel) a step is seen at VBM−0.66 eV due to the contribution from the localized occupied dangling bond. This becomes more pronounced with increasing distance. For positive energies (unoccupied states images, lower panel) the energy dependence is smooth for all distances. A turnover from [001] rows (corrugation ratio >1) to [110] rows (corrugation ratio <1) occurs at about VBM+2.3 eV for larger distances only.

InP(110) surfaces. Similar images for the GaAs(110) surface can be found in Ref. 37. All three materials exhibit essentially the same properties. These are (i) the rotation of the apparent rows formed by the empty states by 90° with increasing magnitude of the positive voltage, (ii) the occupied states change rather little. Only the apparent resolution increases with increasing magnitude of voltage. Figure 21 shows the ratio of the corrugation along the [110] and [001] directions. This ratio reflects the changes in resolution. The corrugation ratio for the occupied states shows two plateaus, a higher one at voltages smaller than −3.5 V and another lower one at voltages larger than −2 V. This change can be understood as the contributions from the localized dangling bond state (A_5 state) and from surface resonances (A_4 states) at the anion shifted and broadened by the effect of the tip-induced band bending (see below). For the empty states the decreasing ratio with increasing voltage reflects the rotation of the rows. [001] oriented rows appear for corrugation ratios >1, i.e., at voltages below 1.7 V for GaP (2.2 V for InP). It can be seen that the rotation is a continuous effect. In addition, the corrugation itself decreases strongly with increasing voltage. The energies are again shifted and broaden by the effect of the tip-induced band bending.

E. Discussion

The experimental data agree very well with the theoretically computed STM images, but only for the largest separation from the surface (Fig. 18). In particular, the rotation of the rows is well reproduced. Also the calculated corrugation ratios have the same trends as the measured ones. Despite this overall agreement the voltage and energy scales do not coincide. This is due to the tip-induced band bending effects. For highly conductive surfaces and metallic tips the voltage V applied to the sample corresponds directly to the energy eV used in the calculation. For semiconductors this is, however, not always the case. The conductivity is too low and thus the tip induces a band bending at the surface due to the effective charging of the surface layer. The band bending depends on the applied voltage, the carrier concentration in the crystal, and on the electronic structure of the surface.[96] For the III-V compounds investigated here the band bending can be estimated, assuming a metallic tip and a potential in the vacuum region consisting of a trapezoidal barrier plus the classical image force term. This calculation has been done for GaAs for a tip-surface separation of 0.9 nm. The result and further details can be found in Ref. 94. It shows that a considerable band bending occurs. A similar band bending occurs on InP(110) surfaces. The band bending modifies the energy scale. For example the corrugation ratio of the occupied states is expected to increase at −0.7 eV. Experimentally it is observed at −3 V on *p*-doped surfaces. At this voltage a band bending of about −2 V is expected. Thus, effectively only states up to 1 eV below the VBM can contribute to the tunnel current at an applied voltage of −3 V. This value agrees rather well with the energy range of the

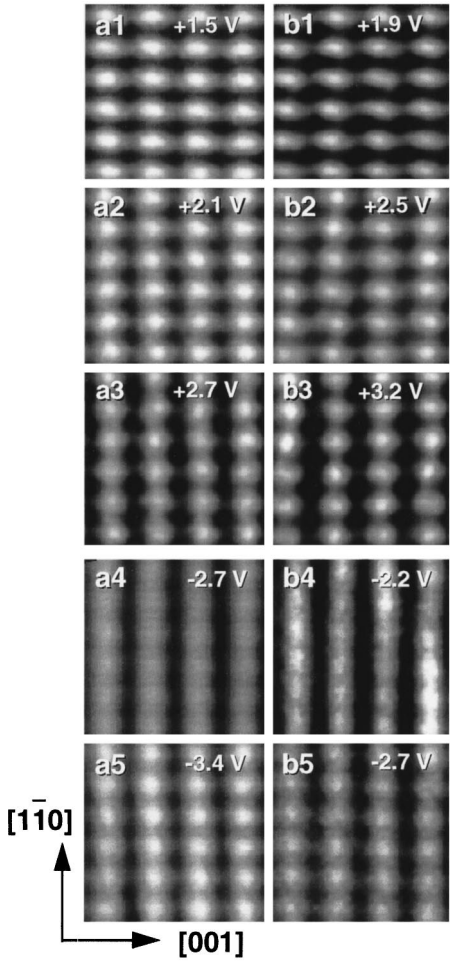

FIG. 20. Experimental STM images of the (110) surface for (a) GaP and (b) InP. Shown are the STM images at different voltages. For positive voltages [unoccupied states images, (1–3)] the pronounced change of the corrugation—from rows in [001] direction at small voltages (1) to rows in [110] direction (3)—can be seen. For negative voltages [occupied states images, (4 and 5)] a small shift of the position of the [110] rows is found.

dangling bond state which shows a maximum DOS at about −0.7 eV (see Figs. 3 and 9). Thus, at low magnitudes of voltage only the occupied dangling bond dominates the images. For larger magnitudes of voltage the contribution of the db state is fully taken into account and the additional small change of the corrugation ratio is due to lower-lying surface resonances. The transition is not as sharp as in the theoretical calculation (Fig. 19), because the tip-induced band bending and the limited energy resolution of the STM smears out the transition.

For the empty states the corrugation ratio starts to change at 1.5–2 V. At this voltage a band bending of 1–1.3 V occurs. Thus the effective energy is about 0.5–0.7 eV above the conduction band minimum. If the band gap of 1.4 eV is taken into account the change occurs 1.9–2.1 eV above the VBM. This agrees with the computed corrugation ratios in Fig. 19. Thus, only at low voltages the empty dangling bond is imaged. At all other voltages an increasing contribution of empty surface resonances occurs, and at large voltages the resonances dominate the images completely.

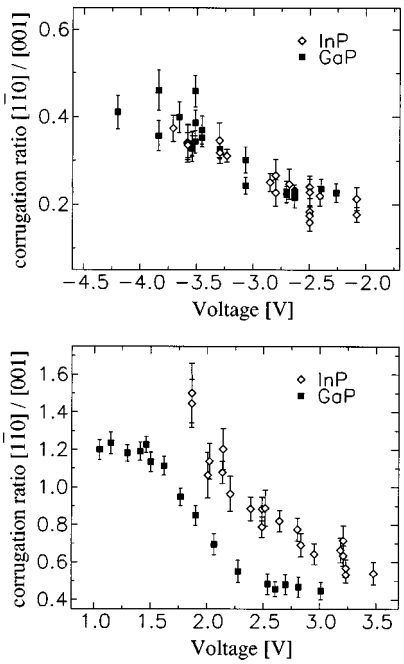

FIG. 21. Experimental corrugation ratios in [$\bar{1}$10] direction and in [001] direction as a function of the applied voltage for InP and GaP. For negative voltages (occupied states images, upper panel) an increase can be seen at about −3 V. For positive voltages (unoccupied states images, lower panel) the turnover from [001] rows (corrugation ratio >1) to [110] rows (corrugation ratio <1) occurs at about 2.2 V in InP and 1.7 V in GaP.

VII. SUMMARY

We compared results of *ab initio* electronic structure calculations using density functional theory with measured STM images for the clean (110) surface of III-V semiconductors. The nature of the wave functions contributing to STM images are analyzed in detail. The atomic structure has been determined by total-energy minimization and the electronic structure has been calculated self-consistently for a slab containing 17 (110) planes separated by a vacuum equivalent to seven (110) planes. Thus the nature of the wave functions (surface localization, surface resonance, or bulklike) for energies in the range of 3 eV on both sides of the fundamental gap has been determined. In particular, the decay of the density profiles into the vacuum as well as into the bulk has been analyzed. A consistent understanding of the voltage-dependent STM images has been obtained: For tunneling out of the occupied states the dangling bond at the anion gives the main contribution for all voltages measured. On the other hand, for tunneling into the empty states the dangling bond at the cation is important only for small voltages. For higher voltages resonances dominate the STM image, yielding the observed rotation of the apparent row direction.

ACKNOWLEDGMENTS

This work was supported in part by the ''Verbundforschung zur Erforschung der Materie mit Synchrotronstrahlung'' of the BMBF. Computations were performed under the grant ''Semiconductor surfaces and interfaces: calculations of the atomic and electronic structure'' on CRAY computers of Forschungszentrum Jülich.

[1] P. Mark, S. C. Chang, W. F. Creighton, and B. W. Lee, Crit. Rev. Solid State Sci. **5**, 189 (1975).
[2] A. R. Lubinsky, C. B. Duke, B. W. Lee, and P. Mark, Phys. Rev. Lett. **36**, 1058 (1976).
[3] C. B. Duke, A. R. Lubinsky, B. W. Lee, and P. Mark, J. Vac. Sci. Technol. **13**, 761 (1976).
[4] S. Y. Tong, A. R. Lubinsky, B. J. Mrstic, and M. A. Van Hove, Phys. Rev. B **17**, 3303 (1978).
[5] A. Kahn, G. Cisneros, M. Bonn, P. Mark, and C. B. Duke, Surf. Sci. **71**, 387 (1978).
[6] A. Kahn, E. So, P. Mark, and C. B. Duke, J. Vac. Sci. Technol. **15**, 580 (1978).
[7] A. Kahn, E. So, P. Mark, C. B. Duke, and R. J. Meyer, J. Vac. Sci. Technol. **15**, 1223 (1978).
[8] R. J. Meyer, C. B. Duke, A. Paton, A. Kahn, E. So, J. L. Jeh, and P. Mark, Phys. Rev. B **19**, 5194 (1979).
[9] C. B. Duke, R. J. Meyer, A. Paton, P. Mark, A. Kahn, E. So, and J. L. Jeh, J. Vac. Sci. Technol. **16**, 1252 (1979).
[10] R. J. Meyer, C. B. Duke, and A. Paton, Surf. Sci. **97**, 512 (1980).
[11] C. B. Duke, R. J. Meyer, A. Paton, J. L. Jeh, J. C. Tsang, A. Kahn, and P. Mark, J. Vac. Sci. Technol. **17**, 501 (1980).
[12] C. B. Duke, R. J. Meyer, and P. Mark, J. Vac. Sci. Technol. **17**, 971 (1980).
[13] C. Mailhiot, C. B. Duke, and D. J. Chadi, Surf. Sci. **149**, 366 (1985).
[14] J. E. Rowe, S. B. Christman, and G. Margaritondo, Phys. Rev. Lett. **35**, 1471 (1975).
[15] W. E. Spicer, P. W. Chye, P. E. Gregory, T. Sukegawa, and I. A. Babalola, J. Vac. Sci. Technol. **13**, 233 (1976).
[16] K. C. Pandey, J. L. Freeouf, and D. E. Eastman, J. Vac. Sci. Technol. **14**, 904 (1977).
[17] K. C. Pandey, J. Vac. Sci. Technol. **15**, 440 (1978).
[18] A. Huijser, J. van Laar, and T. L. van Rooy, Phys. Lett. **65A**, 337 (1978).
[19] L. Sorba, V. Hinkel, H. U. Middelmann, and K. Horn, Phys. Rev. B **36**, 8075 (1987).
[20] P. Chiaradia, M. Fanfoni, P. Nataletti, P. De Padova, L. J. Brillson, M. L. Slade, R. E. Viturro, D. Kilday, and G. Margaritondo, Phys. Rev. B **39**, 5128 (1989).
[21] H. Carstensen, R. Claessen, R. Manzke, and M. Skibowski, Phys. Rev. B **41**, 9880 (1990).
[22] D. J. Chadi, Phys. Rev. B **19**, 2074 (1979).
[23] D. J. Chadi, Phys. Rev. B **18**, 1800 (1978).
[24] D. V. Froehlich, M. E. Lapeyre, J. D. Dow, and R. E. Allen, Superlattices Microstruct. **1**, 87 (1985).
[25] R. M. Feenstra, J. A. Stroscio, J. Tersoff, and A. P. Fein, Phys. Rev. Lett. **58**, 1192 (1987).
[26] L. J. Whitman, J. A. Stroscio, R. A. Dragoset, and R. J. Celotta, Phys. Rev. Lett. **66**, 1338 (1991).
[27] Ph. Ebert, G. Cox, U. Poppe, and K. Urban, Surf. Sci. **271**, 587 (1992).
[28] J. R. Chelikowsky and M. L. Cohen, Phys. Rev. B **13**, 826 (1976).
[29] J. R. Chelikowsky and M. L. Cohen, Phys. Rev. B **20**, 4150 (1979).
[30] A. Zunger, Phys. Rev. B **22**, 959 (1980).
[31] F. Manghi, C. M. Bertoni, C. Calandra, and E. Molinari, Phys. Rev. B **24**, 6029 (1981).
[32] G. P. Srivastava, I. Singh, V. Montgomery, and R. H. Williams, J. Phys. C **16**, 3627 (1983).
[33] S. B. Zhang and M. L. Cohen, Surf. Sci. **172**, 754 (1986).
[34] X. Zhu, S. B. Zhang, S. G. Louie, and M. L. Cohen, Phys. Rev. Lett. **63**, 2112 (1989).
[35] J. L. A. Alves, J. Hebenstreit, and M. Scheffler, Phys. Rev. B **44**, 6188 (1991).
[36] J. M. Bass and C. C. Matthai, Phys. Rev. B **52**, 4712 (1995).
[37] Ph. Ebert, B. Engels, P. Richard, K. Schroeder, S. Blügel, C. Domke, M. Heinrich, and K. Urban, Phys. Rev. Lett. **77**, 2997 (1996).
[38] J. Dąbrowski, H.-J. Müssig, and G. Wolff, Phys. Rev. Lett. **73**, 1660 (1994).
[39] R. M. Feenstra, J. M. Woodall, and G. Pettit, Phys. Rev. Lett. **71**, 1176 (1993).
[40] M. B. Johnson, O. Albreksen, R. M. Feenstra, and H. W. M. Salemink, Appl. Phys. Lett. **63**, 2923 (1993); Erratum, *ibid.* **64**, 1454 (1994).
[41] J. F. Zheng, X. Liu, N. Newman, E. R. Weber, D. F. Ogletree, and M. Salmeron, Phys. Rev. Lett. **72**, 1490 (1994).
[42] G. Lengel, R. Wilkins, G. Brown, M. Weimer, J. Gryko, and R. E. Allen, Phys. Rev. Lett. **72**, 836 (1994).
[43] Ph. Ebert, K. Urban, and M. G. Lagally, Phys. Rev. Lett. **72**, 840 (1994).
[44] Ph. Ebert, M. Heinrich, M. Simon, K. Urban, and M. G. Lagally, Phys. Rev. B **51**, 9696 (1995).
[45] Ph. Ebert, Xun Chen, M. Heinrich, M. Simon, K. Urban, and M. G. Lagally, Phys. Rev. Lett. **76**, 2089 (1996).
[46] K.-J. Chao, A. R. Smith, and C. K. Shih, Phys. Rev. B **53**, 6935 (1996).
[47] Ph. Ebert, M. Heinrich, M. Simon, C. Domke, K. Urban, C. K. Shih, M. B. Webb, and M. G. Lagally, Phys. Rev. B **53**, 4580 (1996).
[48] C. Domke, Ph. Ebert, M. Heinrich, and K. Urban, Phys. Rev. B **54**, 10 288 (1996).
[49] A. R. Smith, K.-J. Chao, C. K. Shih, K. A. Anselm, A. Srinivasan, and B. G. Streetman, Appl. Phys. Lett. **69**, 1214 (1996).
[50] M. C. M. M. van der Wielen, A. J. A. van Roij, and H. van Kempen, Phys. Rev. Lett. **76**, 1075 (1996).
[51] J. Gebauer, R. Krause-Rehberg, C. Domke, Ph. Ebert, and K. Urban, Phys. Rev. Lett. **78**, 3334 (1997).
[52] H. W. M. Salemink, O. Albrektsen, and P. Koenraad, Phys. Rev. B **45**, 6946 (1992).
[53] S. Gwo, K.-J. Chao, C. K. Shih, K. Sadra, and B. G. Streetman, Phys. Rev. Lett. **71**, 1883 (1993).
[54] J. F. Zheng, J. D. Walker, M. B. Salmeron, and E. R. Weber, Phys. Rev. Lett. **72**, 2414 (1994).
[55] R. M. Feenstra, D. A. Collins, D. Z.-Y. Ting, M. W. Wang, and T. C. McGill, Phys. Rev. Lett. **72**, 2749 (1994).
[56] M. Pfister, M. B. Johnson, S. F. Alvarado, H. W. M. Salemink, U. Marti, D. Martin, F. Morier-Genoud, and F. K. Reinhart, Appl. Phys. Lett. **67**, 1459 (1995).
[57] M. B. Johnson, P. M. Koenraad, W. C. van der Vleuten, H. W. M. Salemink, and J. H. Wolter, Phys. Rev. Lett. **75**, 1606 (1995).
[58] S. H. Vosko, L. Wilk, and M. Nusair, Can. J. Phys. **58**, 1200 (1980).
[59] J. Ihm, A. Zunger, and M. L. Cohen, J. Phys. C **12**, 4409 (1979).
[60] P. Richard, B. Engels, K. Schroeder, and S. Blügel (unpublished).
[61] W. E. Davidson, J. Comput. Phys. **17**, 87 (1975); N. Kosugi, *ibid.* **55**, 426 (1984); P. Richard, Ph.D. thesis, RWTH Aachen 1996, published as Forschungszentrum Jülich Report No. 3331 (Jülich, 1996).
[62] D. G. Anderson, J. Assoc. Comput. Mach. **12**, 547 (1964); S. Blügel (unpublished).

[63] R. Fletcher, *Practical Methods of Optimization* (Wiley, New York, 1987).
[64] H. J. Monkhorst and J. D. Pack, Phys. Rev. B **13**, 5188 (1976).
[65] J. D. Pack and H. J. Monkhorst, Phys. Rev. B **16**, 1748 (1977); With the C_{2v} symmetry a planar $4\times4\times1$ and a $4\times4\times2$ **k**-point set both reduce to four **k** points in the irreducible part of the Brillouin zone. For higher accuracy we used the $4\times4\times2$ set.
[66] G. Hörmandinger, J. B. Pendry, F. M. Leibsle, P. W. Murry, R. W. Joyner, and G. Thornton, Phys. Rev. B **48**, 8356 (1993).
[67] S. Heinze and S. Blügel (to be published).
[68] D. Vanderbilt, Phys. Rev. B **32**, 8412 (1985).
[69] B. Engels, Forschungszentrum Jülich, Report No. 3215, 1996 (unpublished).
[70] J. Tersoff and D. R. Hamann, Phys. Rev. Lett. **50**, 1998 (1983).
[71] J. Bardeen, Phys. Rev. Lett. **6**, 57 (1961).
[72] C. J. Chen, in *Introduction to Scanning Tunneling Microscopy*, edited by M. Lapp, J. Nishizawa, B. B. Snavely, H. Stark, A. C. Tam, and T. Wilson, Oxford Series in Optical and Imaging Sciences Vol. 4 (Oxford University Press, New York, 1993).
[73] W. Mönch, in *Semiconductor Surfaces and Interfaces*, edited by G. Ertl, R. Gomer, and D. L. Mills, Springer Series in Chemical Physics and Physics of Surfaces Vol. 26 (Springer, Berlin, 1993), p. 115.
[74] N. D. Lang, Phys. Rev. B **34**, 5947 (1986).
[75] P. J. Jennings, R. O. Jones, and M. Weinert, Phys. Rev. B **37**, 6113 (1988); R. O. Jones and P. J. Jennings, Surf. Sci. Rep. **9**, 165 (1988).
[76] K. Besocke, Surf. Sci. **181**, 145 (1987).
[77] A. Kahn, Surf. Sci. Rep. **3**, 193 (1983).
[78] C. A. Swarts, T. C. McGill, and W. A. Goddard III, Surf. Sci. **110**, 400 (1981).
[79] C. B. Duke, A. Paton, A. Kahn, and C. R. Bonapace, Phys. Rev. B **27**, 6189 (1983).
[80] A. Kahn, Surf. Sci. **168**, 1 (1986).
[81] J. Fritsch and P. Pavone, Surf. Sci. **344**, 159 (1995).
[82] J. E. Northrup, Phys. Rev. B **47**, 10 032 (1993).
[83] A. McKinley, G. P. Srivastava, and R. H. Williams, J. Phys. C **13**, 1581 (1980).
[84] C. Janowitz, R. Manzke, M. Skibowski, Y. Takeda, Y. Miyamoto, and K. Cho, Surf. Sci. Lett. **275**, L669 (1992).
[85] T. Riesterer, P. Perfetti, M. Tschudy, and B. Reihl, Surf. Sci. **189/190**, 795 (1987).
[86] B. Reihl, T. Riesterer, M. Tschudy, and P. Perfetti, Phys. Rev. B **38**, 13 456 (1988).
[87] J. M. Nicholls, K. O. Magnusson, and B. Reihl, Surf. Sci. Lett. **243**, L31 (1991).
[88] G.-X. Qian, R. M. Martin, and D. J. Chadi, Phys. Rev. B **37**, 1303 (1988).
[89] R. Möller, J. Fraxedas, C. Baur, B. Koslowski, and K. Dransfeld, Surf. Sci. **269/270**, 817 (1992). A bridgebond is shown in Fig. 1, but labeled backbond. It should be read as bridgebond [B. Koslowski (private communication)].
[90] R. Möller, C. Baur, A. Esslinger, U. Graf, and P. Kürz, Nanotechnology **1**, 50 (1990).
[91] R. M. Feenstra, Phys. Rev. B **50**, 4561 (1994).
[92] P. Mårtensson and R. M. Feenstra, Phys. Rev. B **39**, 7744 (1989).
[93] A. J. Heinrich, M. Wenderoth, M. A. Rosentreter, M. A. Schneider, and R. G. Ulbrich, Appl. Phys. Lett. **70**, 449 (1997).
[94] R. M. Feenstra and J. A. Stroscio, J. Vac. Sci. Technol. B **5**, 923 (1987).
[95] C. J. Chen and R. J. Hamers, J. Vac. Sci. Technol. B **9**, 503 (1991).
[96] M. McEllistrem, G. Haase, D. Chen, and R. J. Hamers, Phys. Rev. Lett. **70**, 2471 (1993).